Rhenium-Based Molecular Rectangles as Frameworks for Ligand-Centered Mixed Valency and Optical Electron Transfer

Peter H. Dinolfo, Mary Elizabeth Williams, Charlotte L. Stern, and Joseph T. Hupp*

Contribution from the Department of Chemistry, 2145 Sheridan Road, Northwestern University, Evanston, Illinois 60208-3113

Received May 7, 2004; E-mail: jthupp@chem.northwestern.edu

Abstract: A series of six neutral, tetrametallic, molecular rectangles has been synthesized that have the form ([Re(CO)$_3$]$_2$BiBzIm)$_2$-μ,μ'-(LL)$_2$, where BiBzIm is 2,2'-bisbenzimidazolate and LL is a reducible, dipyridyl or diazine ligand. X-ray crystallographic studies of the six show that the rectangle frameworks, as defined by the metal atoms, range in size from 5.7 Å × 7.2 Å to 5.7 Å × 19.8 Å. The singly reduced rectangles are members of an unusual category of mixed-valence compounds in which the ligands themselves are the redox centers and interligand electronic communication is controlled by direct ligand orbital overlap rather than by superexchange through the metal ions. Despite nominally identical coordination-defined ligand positioning, the spectrally determined electronic strengths, H_{ab}^2, vary by roughly 100-fold. As shown by X-ray crystallography and computational modeling, the observed differences largely reflect detailed geometric configurational differences that can either facilitate or frustrate productive direct orbital overlap.

Introduction

Molecular rectangles comprise one subset of a now quite large collection of discrete cavity-containing supramolecular assemblies (squares, triangles, prisms, etc.) obtainable via metal-ion coordination chemistry.[1-5] Recently we reported on the synthesis of rectangles featuring rhenium(I) sites organized in pairs by doubly chelating planar ligands such as 2,2'-bisbenzimidazolate and then linked by rigid or semirigid difunctional ligands (LL) such as 4,4'-bipyridine to close the cycle.[6] Notably, the 4,4'-bipyridine (bpy) containing rectangles exhibit well-defined LL electrochemistry; depending on solvent, as many as four electrons can be added in stepwise fashion with retention of the rectangular configuration. Other examples of transition-metal based rectangles include a tetrarhenium compound featuring alternating pyrazine and bpy edges,[7,8] tetrarhenium compounds having bridging thiolates[9] or alkoxides[10,11] along the short edges, and tetraplatinum compounds joined on the short edge with anthracene.[12-15]

While the cavities of the new rectangles are too narrow to encapsulate guest molecules, they are of finite width, with LL/LL separation distances exceeding van der Waals contact distances by ca. 1.5 to 2 Å, at least at the coordination sites. We reasoned that the close proximity would facilitate through-space electronic communication between ligands, potentially to a much greater degree than coordination-bond-mediated interactions (superexchange interactions). At the same time the metal frameworks should define reasonably fixed cofacial ligand geometries. To evaluate LL/LL electronic communication, we have examined the rectangles spectroelectrochemically in the 1− charge state, i.e., a mixed-valence (MV) state with respect to the ligands, LL. We find for most, but not all, of the assemblies that electronic interactions are observable and their strength is measurable based on the appearance of broad absorption bands in the near-infrared region assignable as intervalence transitions (IT), eq 1. IT band energies and shapes can provide information about electronic coupling energies (H_{ab}), reorganization energies (λ), and activation free energies (ΔG^*) for the corresponding thermal electron exchange reaction.

It is worth noting that most mixed-valence coordination compounds feature metal ions rather than ligands as electron donors and acceptors.[16-22] Especially for second and third row transition metals, the multiplicity of d orbitals, mixed and split
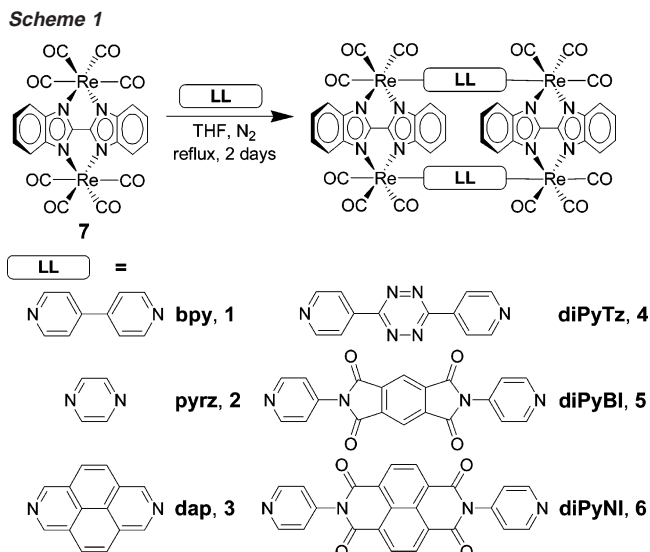
(1) Leininger, S.; Olenyuk, B.; Stang, P. J. *Chem. Rev.* **2000**, *100*, 853−907.
(2) Stang, P. J.; Olenyuk, B. *Acc. Chem. Res.* **1997**, *30*, 502−518.
(3) Fujita, M. *Chem. Soc. Rev.* **1998**, *27*, 417−425.
(4) Holliday, B. J.; Mirkin, C. A. *Angew. Chem., Int. Ed.* **2001**, *40*, 2022−2043.
(5) Cotton, F. A.; Lin, C.; Murillo, C. A. *Acc. Chem. Res.* **2001**, *34*, 759−771.
(6) Benkstein, K. D.; Hupp, J. T.; Stern, C. L. *Angew. Chem., Int. Ed.* **2000**, *39*, 2891−2893.
(7) Rajendran, T.; Manimaran, B.; Liao, R.-T.; Lin, R.-J.; Thanasekaran, P.; Lee, G.-H.; Peng, S.-M.; Liu, Y.-H.; Chang, I. J.; Rajagopal, S.; Lu, K.-L. *Inorg. Chem.* **2003**, *42*, 6388−6394.
(8) Rajendran, T.; Manimaran, B.; Lee, F.-Y.; Lee, G.-H.; Peng, S.-M.; Wang, C. M.; Lu, K.-L. *Inorg. Chem.* **2000**, *39*, 2016−2017.
(9) Benkstein, K. D.; Hupp, J. T.; Stern, C. L. *Inorg. Chem.* **1998**, *37*, 5404−5405.
(10) Manimaran, B.; Rajendran, T.; Lu, Y.-L.; Lee, G.-H.; Peng, S.-M.; Lu, K.-L. *J. Chem. Soc., Dalton Trans.* **2001**, 515−517.
(11) Woessner, S. M.; Helms, J. B.; Shen, Y.; Sullivan, B. P. *Inorg. Chem.* **1998**, *37*, 5406−5407.
(12) Das, N.; Mukherjee, P. S.; Arif, A. M.; Stang, P. J. *J. Am. Chem. Soc.* **2003**, *125*, 13950−13951.
(13) Kaim, W.; Schwederski, B.; Dogan, A.; Fiedler, J.; Kuehl, C. J.; Stang, P. J. *Inorg. Chem.* **2002**, *41*, 4025−4028.
(14) Kuehl, C. J.; Huang, S. D.; Stang, P. J. *J. Am. Chem. Soc.* **2001**, *123*, 9634−9641.
(15) Kuehl, C. J.; Mayne, C. L.; Arif, A. M.; Stang, P. J. *Org. Lett.* **2000**, *2*, 3727−3729.
(16) Creutz, C. *Prog. Inorg. Chem.* **1983**, *30*, 1−73.
(17) Robin, M. B.; Day, P. *Adv. Inorg. Chem. Radiochem.* **1967**, *10*, 247−422.
(18) Crutchley, R. J. *Adv. Inorg. Chem.* **1994**, *41*, 273−325.
(19) Kaim, W.; Klein, A.; Gloeckle, M. *Acc. Chem. Res.* **2000**, *33*, 755−763.
(20) Demadis, K. D.; Hartshorn, C. M.; Meyer, T. J. *Chem. Rev.* **2001**, *101*, 2655−2685.

(1)
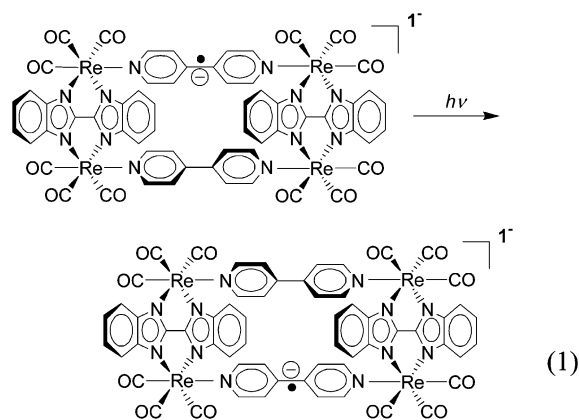
in energy by spin−orbit coupling, typically leads to multiple, overlapping IT bands. The multiplicity and overlap can complicate the estimation of H_{ab}, λ, and ΔG^* from band properties. These complications should be absent for the rectangle-based MV assemblies, as well as for most other ligand-centered mixed valence (LCMV) compounds. Among the few examples of LCMV compounds known to display measurable intervalence absorptions are singly and doubly reduced tris-2,2′-bipyridyl complexes of Ru and Ir.[23,24] These are characterized by relatively weak IT bands ($\epsilon < 400$ M^{-1} cm^{-1}), a consequence of geometric orthogonality (i.e., 90° orientation) of the planar donor ligand and each of two acceptor ligands. Also displaying observable but weak IT bands is [Os^{III}(bpy^0)$_2$(bpy$^-$)]$^{2+*}$, the lowest energy excited-state form of this compound.[20] Kitagawa and co-workers have described a series of LCMV compounds, [Cr^{III}(X$_4$SQ)$_{3-n}$-(X$_4$Cat)$_n$]$^{-n}$ (SQ = semiquinonate, Cat = catecholate, X = Br and Cl, $n = 0$, 1, and 2), which have strong IT bands between 4500 and 6000 cm^{-1}, mediated by the Cr^{III} ions linking the ligands.[25−27] Recently Pratt and Stack have observed intense ($\epsilon \approx 2500$ M^{-1} cm^{-1}) and moderately asymmetric IT bands for two Cu salen compounds in their singly oxidized form where the phenolic moieties on each side of the complex act as the redox centers.[28]

We find that the electronic interactions within the rectangle-based MV assemblies are indeed dominated by direct through-space LL/LL interactions rather than bond-mediated interactions. Thus the rectangles comprise relatively rare examples of MV systems that are describable by single-transition, two-state treatments (as opposed to the three- and four-state treatments appropriate for superexchange based electronic communication and the multitransition treatments appropriate for metal-based systems[29]). From Hush's classical two-state theory, the available mixed-valent rectangles span the range from essentially Class I (noncommunicating, fully valence-localized redox centers) to

(21) Ito, T.; Hamaguchi, T.; Nagino, H.; Yamaguchi, T.; Kido, H.; Zavarine, I. S.; Richmond, T.; Washington, J.; Kubiak, C. P. *J. Am. Chem. Soc.* **1999**, *121*, 4625−4632.
(22) Elliott, C. M.; Derr, D. L.; Matyushov, D. V.; Newton, M. D. *J. Am. Chem. Soc.* **1998**, *120*, 11714−11726.
(23) Heath, G. A.; Yellowlees, L. J.; Braterman, P. S. *Chem. Phys. Lett.* **1982**, *92*, 646−648.
(24) Coombe, V. T.; Heath, G. A.; MacKenzie, A. J.; Yellowlees, L. J. *Inorg. Chem.* **1984**, *23*, 3423−3425.
(25) Chang, H.-C.; Kitagawa, S. *Angew. Chem., Int. Ed.* **2002**, *41*, 130−133.
(26) Chang, H.-C.; Mochizuki, K.; Kitagawa, S. *Inorg. Chem.* **2002**, *41*, 4444−4452.
(27) Chang, H.-C.; Miyasaka, H.; Kitagawa, S. *Inorg. Chem.* **2001**, *40*, 146−156.
(28) Pratt, R. C.; Stack, T. D. P. *J. Am. Chem. Soc.* **2003**, *125*, 8716−8717.
(29) Brunschwig, B. S.; Creutz, C.; Sutin, N. *Chem. Soc. Rev.* **2002**, *31*, 168−184.

Scheme 1

Class II or borderline Class III (valence delocalized) on the Robin and Day[17] scale. Reported below are the syntheses, X-ray crystal structures (neutral form), electrochemistry, and electronic and vibrational spectroscopy of these compounds.

Results and Discussion

Synthesis and Initial Characterization. The general synthesis of rectangles **1**−**6** is shown in Scheme 1 (abbreviations correspond to ligand names, and numbers represent rectangles).[6,30,31] Equivalent quantities of [Re(CO)$_4$]$_2$BiBzIm (**7**) (BiBzIm = 2,2′-bisbenzimidazolate) and redox-active ligand, LL, are refluxed in THF for 48 h. The resulting supramolecular complexes are typically isolated in 43−96% yield.

The reactivity of **7** is an example of the well-known translabilization effect of carbonyl ligands of Group VII complexes.[32−35] Reactions of this kind generally proceed through a dissociative route. The substitution inertness of the doubly chelating BiBzIm^{2-} ligand, however, ensures that only one coordination site per metal is opened, in this case cis to the chelating ligand.[36−38] The relatively high yields of closed cycles (rectangles) point to the involvement of solvento complexes as intermediates and equilibration to reach thermodynamic products: stable rectangular structures. ^{1}H NMR, IR, and MS data are consistent with the formation of discrete, highly symmetrical, cycles and not open oligomers. Presumably, any partially reacted or polymerized compounds remain in the reaction solution as solvento species.

Figure 1 shows the carbonyl stretching region of the IR spectra for **7**, **2**, and **4**. Four bands are present for **7**, consistent with D_{2h} symmetry. The spectrum for **2** shows only three CO stretching bands, consistent with D_{2h} symmetry. For rectangles larger than **2**, the local symmetry of the [Re(CO)$_3$]$_2$BiBzIm

(30) Benkstein, K. D.; Hupp, J. T.; Stern, C. L. *J. Am. Chem. Soc.* **1998**, *120*, 12982−12983.
(31) Benkstein, K. D.; Stern, C. L.; Splan, K. E.; Johnson, R. C.; Walters, K. A.; Vanhelmont, F. W. M.; Hupp, J. T. *Eur. J. Inorg. Chem.* **2002**, *2002*, 2818−2822.
(32) Abel, E. W.; Wilkinson, G. *J. Chem. Soc.* **1959**, 1501−1505.
(33) Wojcicki, A.; Basolo, F. *J. Am. Chem. Soc.* **1961**, *83*, 525−528.
(34) Angelici, R. J.; Basolo, F. *J. Am. Chem. Soc.* **1962**, *84*, 2495−2499.
(35) Angelici, R. J.; Basolo, F. *Inorg. Chem.* **1963**, *2*, 728−731.
(36) Atwood, J. D.; Brown, T. L. *J. Am. Chem. Soc.* **1976**, *98*, 3160−3166.
(37) Dobson, G. R. *Acc. Chem. Res.* **1976**, *9*, 300−306.
(38) Lichtenberger, D. L.; Brown, T. L. *J. Am. Chem. Soc.* **1978**, *100*, 366−373.

Table 1. Crystallographic Data for **1**−**6**

compound	1	2	3	4	5	6
empirical formula	$Re_4C_{75}H_{62}$-$N_{12}O_{15.75}$	$Re_2C_{27.5}H_{14}Cl$-N_6O_6	$Re_4C_{78}H_{47}Cl_4$-$N_{12}O_{14}$	$Re_4C_{64}H_{32}$-$N_{20}O_{12}$	$Re_4C_{135.5}H_{36}$-$N_{16}O_{20}$	$Re_4C_{94}H_{52}$-$N_{16}O_{24}S_2$
formula weight	2128.2	932.3	2262.9	2017.9	2952.6	2598.44
crystal color, habit	yellow, block	red, block	yellow, needle	red, block	yellow, block	orange, needle
crystal dimensions (mm³)	0.102 × 0.056 × 0.044	0.180 × 0.166 × 0.080	0.412 × 0.050 × 0.026	0.284 × 0.222 × 0.158	0.212 × 0.148 × 0.118	0.456 × 0.032 × 0.030
crystal system	monoclinic	monoclinic	monoclinic	tetragonal	monoclinic	monoclinic
space group	$P21/c$	$P21/n$	$P21/c$	$I41/a$	$P21/n$	$P21/n$
a (Å)	12.3741(10)	13.830(3)	12.401(4)	30.8925(11)	10.9266(19)	11.000(3)
b (Å)	48.753(4)	13.299(3)	11.578(3)	30.8925(11)	22.014(4)	22.681(7)
c (Å)	24.198(2)	19.931(5)	26.649(8)	26.6992(13)	29.322(5)	19.552(6)
β (deg)	93.262(2)	101.335(4)	97.184(5)	91.420(3)	94.151(5)	
V (Å³)	14575(2)	3594.4(15)	3796.2(19)	25480.3(18)	7051(2)	4865(3)
Z	8	4	2	8	2	2
T [K]	153	153	153	153	153	153
ρ (calcd, g/cm³)	1.94	1.723	1.980	1.052	1.391	1.774
μ (cm⁻¹)	6.699	6.846	6.571	3.828	3.487	5.084
goodness-of-fit on F^2	0.968	1.047	1.065	1.027	1.071	0.875
R^a	0.0783	0.0527	0.0496	0.0665	0.0508	0.0640
$R_w{}^b$	0.1490	0.1654	0.1451	0.2873	0.1604	0.1795

^{a} $R(F) = (\Sigma F_o - F_c)/\Sigma F_o$. ^{b} $R_w(F_o^2) = [\Sigma[w(F_o^2 - F_c^2)^2]/\Sigma w F_o^4]^{1/2}$.
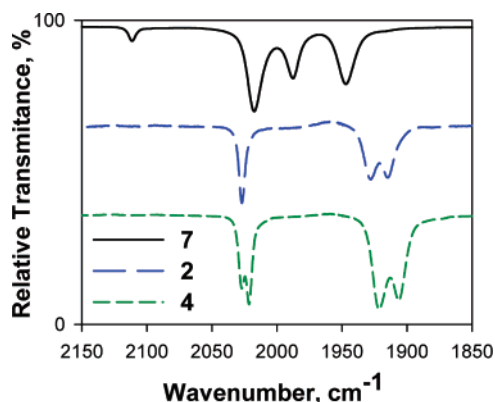
Figure 1. Carbonyl stretching region of the infrared spectra for **7** (solid black line, top), **2** (long dashed blue line, middle), and **4** (short dashed green line, bottom) taken in THF.

edges, C_{2v}, governs the spectral behavior and the higher energy transition is split, such that four distinct CO stretching bands are observed for **3**−**6**. ¹H NMR spectra of **2**−**6** are also consistent with the formation of highly symmetrical rectangular structures. Upon rectangle formation, the α and β protons of coordinated BiBzIm shift upfield by approximately 0.15 ppm, while the resonances of the LL species generally shift downfield. Only one set of LL proton resonances and one set of BiBzIm resonances are seen for each assembly, consistent with the formation of highly symmetrical closed cycles.
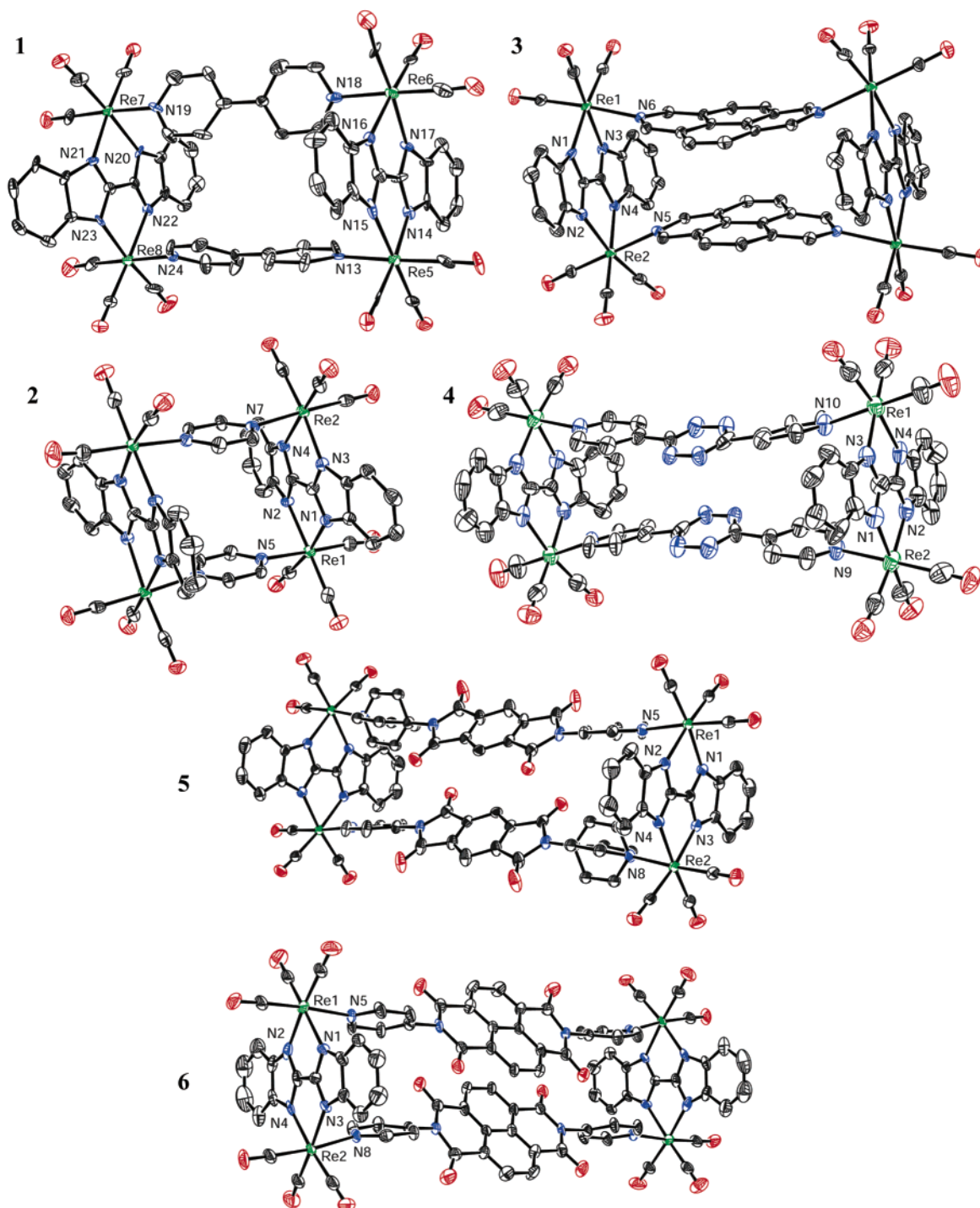
X-ray Crystal Structures. ORTEP drawings of the single-crystal X-ray structures of **1**−**6** are shown in Figure 2. The structures were solved by direct methods and corroborate the proposed molecular structures. Table 1 contains crystal information and refinement data. Table 2 lists representative Re−N bond lengths. Common to the structure of all but the smallest assembly are distortions from rectangular box geometries such that the LL pairs achieve van der Waals contact. We have previously observed an extreme example, based on pyridyl

ethynl porphyrin ligands where van der Waals contact is achieved over nearly the entire porphyrinic area of the LL/LL pair.[31]

The crystal structure of **1** contains two distinct but very similar rectangles in the asymmetric unit, both of which have dimensions of 11.5 Å × 5.7 Å as defined by the Re atoms.[39] These are slightly larger than those found previously for the Mn analogue (11.2 Å × 5.5 Å).[6] Comparison of the structures of **1** and the Mn analogue[6] shows that the dimensional differences reflect both metal−ligand bond length and ligand geometry differences. In **1**, the Re−N bond lengths are approximately 0.1 Å longer than that of the Mn−N bond lengths which accounts for the 0.2 Å difference along the short edge and part of the 0.3 Å difference for the long edge. For the Mn version, a near zero dihedral angle exists for the pair of rings comprising each bipyridine ligand. The bpy ligands, however, bow inward, thereby reducing the Mn−Mn separation distances along the long edges of the rectangle.

The differences between the two crystallographic isomers of **1** are due to slight variations in the orientation of the bpy ligands within the rectangular cycle. Curiously, the bpy rings in the Mn analogue are essentially planar (dihedral angle between the pyridine rings is less than 10°), while, in **1**, the dihedral angles range from 30° to 40°, values similar to those of unconstrained biphenyl and 4,4′-bipyridyl compounds. The collinearity of the pyridines within each twisted bpy ligand serves to place at a maximum possible separation distance the pairs of Re atoms defining the long edges of the rectangle. In the rectangle environment, the dihedral twist serves to bring the otherwise cofacial pyridyl rings of the pair of bpy ligands into van der Waals contact (~3.8 Å closest C−C distance). The geometry around the Re atoms is distorted octahedral; the angles between

(39) Benkstein, K. D. *The Design, Synthesis and Evaluation of Transition Metal-Based Cyclophanes for Host: Guest Applications.* Ph.D. Thesis, Northwestern University, Evanston, IL, 2000.

Figure 2. ORTEP drawings for the crystal structures of **1-6**. Carbon atoms are shown in black, nitrogen in blue, oxygen in red and rhenium in green; the hydrogen atoms and solvent molecules were removed for clarity. Displacement ellipsoids are drawn at the 50% probability level for **1**, 40% for **2**, **3**, **5**, and **6**, and 30% for **4**. The figure for **1** displays only one of the two rectangles present in the asymmetric unit.

the imidazolyl and pyridyl nitrogens (N–Re–N) range from 80.1° to 89.1°. The unit cell also contains eight disordered THF molecules.

The structure of **2**, in contrast to **1**, is characterized by a uniform LL/LL spacing (~5.3 Å), reflecting the rigidity of the cofacial pyrazine ligands. The rectangle framework dimensions, as defined by the Re atoms, are 7.2 Å × 5.7 Å. Similar to **1**, the geometry of the Re coordination sphere is distorted octahedral. The angles between the BiBzIm nitrogens and the bpy pyridyl nitrogens (N–Re–N) range from 83.4° to 84.3°.

Somewhat different from the rest of the rectangles is an outward bending of the BiBzIm chelating ligands, which also effects the distortion of the Re centers. The X-ray measurements additionally show that the unit cell of **2** contains disordered dichloroethane and THF molecules.

The structures of **3** and **4** comprise moderately distorted rectangles. The greater length of the diPyTz and dap ligands, and the ease which coplanarity of ligand rings can be achieved, allow LL pairs to come within van der Waals contact. The framework dimensions of **3** and **4**, as determined by the Re

Table 2. Re–N Bond Distances for **1**–**6**

	LL pyridyl N–Re		imidazolyl N–Re	
		bond lengths (Å)		
1	Re1–N1	2.208(10)	Re1–N2	2.207(10)
			Re1–N3	2.235(11)
	Re2–N6	2.259(12)	Re2–N4	2.199(11)
			Re2–N5	2.216(11)
	Re3–N7	2.212(10)	Re3–N8	2.195(10)
			Re3–N9	2.199(10)
	Re4–N12	2.215(11)	Re4–N10	2.191(11)
			Re4–N11	2.215(10)
	Re5–N13	2.199(11)	Re5–N14	2.197(11)
			Re5–N15	2.167(12)
	Re6–N18	2.233(12)	Re6–N16	2.218(10)
			Re6–N17	2.194(10)
	Re7–N19	2.233(11)	Re7–N20	2.202(10)
			Re7–N21	2.199(11)
	Re8–N24	2.200(10)	Re8–N22	2.227(10)
			Re8–N23	2.258(11)
2	Re1–N5	2.196(7)	Re1–N1	2.210(8)
			Re1–N2	2.200(7)
	Re2–N7	2.205(7)	Re2–N3	2.220(7)
			Re2–N4	2.211(8)
3	Re1–N6	2.229(6)	Re1–N1	2.213(7)
			Re1–N3	2.218(6)
	Re2–N5	2.231(7)	Re2–N2	2.218(6)
			Re2–N4	2.199(7)
4	Re1–N10	2.216(9)	Re1–N3	2.220(10)
			Re1–N4	2.259(10)
	Re2–N9	2.229(9)	Re2–N1	2.242(10)
			Re2–N2	2.226(11)
5	Re1–N5	2.210(5)	Re1–N1	2.217(6)
			Re1–N2	2.221(6)
	Re2–N8	2.222(5)	Re2–N4	2.210(6)
			Re2–N3	2.213(6)
6	Re1–N5	2.222(10)	Re1–N1	2.246(11)
			Re1–N2	2.200(13)
	Re2–N8	2.218(10)	Re2–N3	2.192(10)
			Re2–N4	2.156(12)

atoms, are 11.2 Å × 5.7 Å and 15.3 Å × 5.7 Å, respectively. While more extreme in the case of **4**, the inward bowing of LL ligands distorts the Re–BiBzIm short edges of both rectangles, drawing the Re atoms toward the center of the molecule.

As a result of the bend in the central dap ligand, the geometries around the Re centers in **3** are distorted octahedral. The angles between nitrogens of the BiBzIm and the diazapyrene ligands (N–Re–N) range from 80.0° to 84.5°, while the angles between the BiBzIm nitrogens and the axial carbonyl ligands (N–Re–C) are somewhat enlarged (94.8° to 97.5°), consistent with an inward displacement of the Re atoms. Along with the displacement of the Re centers, the BiBzIm ligand is curved toward the center of the complex, with a mean deviation of 0.1 Å as defined by a plane through the BiBzIm bridge. The unit cell of **3** contains one disordered 1,2-dichloroethane and one disordered THF molecule.

In addition to the inward bending of the diPyTz ligands of **4**, the central tetrazine rings are twisted slightly in relation to the Re coordinating pyridine units (ca. 10–15°). This twist facilitates the attainment of LL/LL van der Waals contact while minimizing the need for further bending of the diPyTz ligand and distortion of the rectangular shape. The residual distortion of the octahedral Re centers is similar to that of **3**; the angles between nitrogens of the BiBzIm and the diazapyrene ligands (N–Re–N) range from 81.0° to 83.8°, while the angles between the BiBzIm nitrogens and the axial carbonyl ligands (N–Re–C) range from 95.1° to 98.0°. Unlike the rest of the

rectangles, the unit cell of **4** does not contain any additional solvent molecules.

Single-crystal X-ray studies of **5** and **6** reveal similar structures, in which the central benzene tetracarboxidiimide and naphthalene tetracarboxidiimide rings are rotated in relation to the Re coordinating pyridine groups (dihedral angles of ca. 45° for **5** and ca. 55° for **6**). The rotation allows the central rings to reach van der Waals contact while retaining linearity along the N–N–N–N ligand axis and avoiding the highly compressed structures seen for **3** and **4**. The dihedral displacements also facilitate horizontal offsets of the central rings, such that less than 25% and 40% cofacial area overlaps are attained for the central portions of the ligands for **5** and **6**, respectively. Offsets of this kind are characteristic of π-stacking interactions, placing comparatively electron-deficient hydrogens in close proximity to the central electron-rich sections of the neighboring aromatic rings. In **5**, there is disorder in one of the pyridine units, such that the ring is orientated either parallel (66% occupancy) or orthogonal (34%) to the Re–Re plane. There does exist a slight inward bending of the ligands that effects the geometry of the Re centers. The angles between of the imidazolyl and pyridyl nitrogens in **5** (N–Re–N) range from 83.2° to 85.8°, while these angles in **6** range from 81.5° to 84.4°. In addition, the unit cell of **5** contains six disordered THF molecules, and **6** contains three disordered MeOH molecules and one disordered DMSO molecule. The framework dimensions of **5** and **6**, as determined by there Re atoms, is 19.5 Å × 5.7 Å and 19.8 Å × 5.7 Å, respectively.

Notable, across the series of **1**–**6** are the similarities of the Re–N bond distances for both the pyridyl and imidazolyl nitrogens, each with averages of 2.2 Å. These values are close to those of other pyridyl-Re(CO)$_3$ compounds[40–42] and a previously reported porphyrinic based rectangle.[31] The similar Re–N bond lengths for pyridyl versus imidazolyl nitrogens suggest that the BiBzIm remains largely dianionic and does not contribute enormous electron density to the cationic Re atoms.

Electrochemistry. Cyclic voltammograms (CV) of **1**–**6** display chemically reversible reduction waves; representative CVs of **2**, **3**, and **4** are shown in Figure 3. Similar behavior has been noted previously for **1** and related compounds.[6,9–11,13,31,43] The waves are assigned as one-electron reduction reactions of the LL ligands. Stepwise reduction of identical ligands reflects, in part, the electrostatic cost of creating a negatively charged ligand (or making an already negatively charged ligand more negative) in the presence of another negatively charged ligand. No oxidative waves are observed for **1**–**6** within the solvent windows.

Table 3 lists reduction potentials for **1**–**6** and the corresponding free LL species versus ferrocenium/ferrocene, a reference couple whose potential should be largely independent of solvent composition. The ligand reductions for the rectangular assemblies are shifted to substantially less negative potentials in comparison with free ligands.[44–46] The differences are consistent

(40) Bélanger, S.; Hupp, J. T.; Stern, C. L. *Acta Crystallogr., Sect. C: Cryst. Struct. Commun.* **1998**, *C54*, 1596–1600.
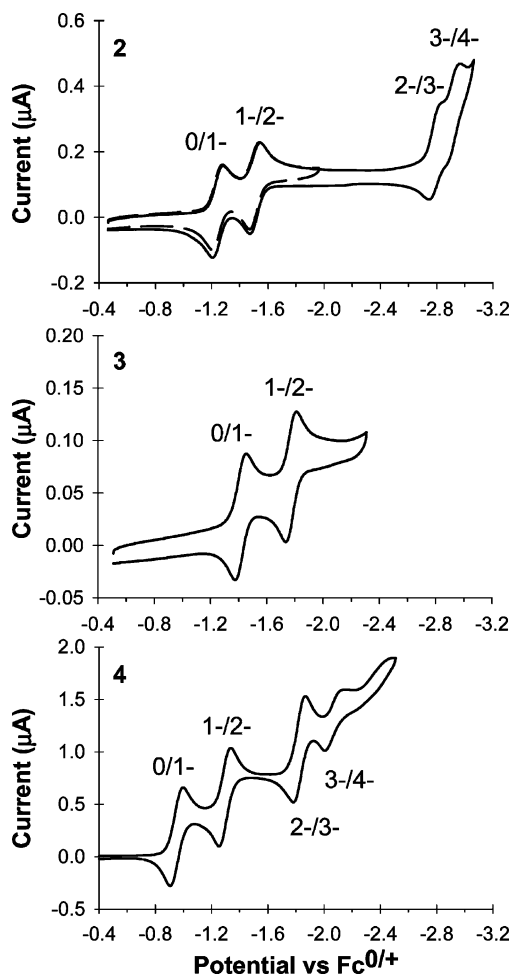(41) Bélanger, S.; Hupp, J. T.; Stern, C. L.; Slone, R. V.; Watson, D. F.; Carrell, T. G. *J. Am. Chem. Soc.* **1999**, *121*, 557–563.
(42) Slone, R. V.; Hupp, J. T.; Stern, C. L.; Albrecht-Schmitt, T. E. *Inorg. Chem.* **1996**, *35*, 4096–4097.
(43) Hartmann, H.; Berger, S.; Winter, R.; Fiedler, J.; Kaim, W. *Inorg. Chem.* **2000**, *39*, 4977–4980.
(44) Braterman, P. S.; Song, J. I. *J. Org. Chem.* **1991**, *56*, 4678–4682.
(45) O'Reilly, J. E.; Elving, P. J. *J. Am. Chem. Soc.* **1972**, *94*, 7941–7949.

Figure 3. Cyclic voltammograms of **2** (top), **3** (middle), and **4** (bottom) in THF with 0.1 M TBAPF$_6$ as the supporting electrolyte.

Figure 4. UV−visible absorption data for the neutral (solid black line), 1− (long dashed green line), and 2− (short dashed blue line) states for **1** and **2** taken in THF, with 0.1 M TBAPF$_6$ as the supporting electrolyte.

Table 3. Reduction Potentials (V vs Fc/Fc+)

rectangle	$E^{0/1-}_{1/2}$	$E^{1-/2-}_{1/2}$	$E^{2-/3-}_{1/2}$	$E^{3-/4-}_{1/2}$	K_c^{1-}	K_c^{3-}	solvent^a
1^b	−1.47	−1.70	−2.28	−2.43	7.7×10^3	3.0×10^2	THF
2	−1.23	−1.48	−2.76	−2.89	3.7×10^4	2.0×10^2	THF
3	−1.56	−1.92			1.2×10^6		THF
4	−0.95	−1.30	−1.82	−2.08	8.2×10^5	2.5×10^4	THF
5	−0.86	−1.11			1.7×10^4		THF
6	−0.70	−0.79	−1.33^c		30		DMSO

LL ligand	$E^{0/1-}_{1/2}$	$E^{1-/2-}_{1/2}$	solvent^a
bpy^d	−2.39	−2.88	DMF
pyrz^e	−2.47^g		CH$_3$CN
dap	−2.39		THF
diPyTz	−1.81	−2.50	THF
diPyBI^f	−1.02^g	−1.68^g	DMF
diPyNI^f	−0.79^g	−1.30^g	DMF

^{a} 0.1 M TBAPF6 used as supporting electrolyte. ^{b} Values taken from ref 6. ^{c} 2−/3− and 3−/4− waves strongly overlap. ^{d} Values taken from ref 44. ^{e} Value taken from ref 45. ^{f} Values from di-(2,5-di-*tert*-butylphenyl)-substituted tetracarboximide dianhydrides used in place of dipyridyl complexes, taken from ref 46. ^{g} Converted to Fc$^{0/+}$ reference by subtracting 0.31 from reported value referenced to SCE.

with the expectation of electrostatic stabilization of the negatively charged, reduced forms of the ligands by the coordinated rhenium cations. The positive shifts are smaller for **5** and **6**, most likely due to isolation of charge on the central tetra-carboxydimide dianhydrides and away from the nominally

(46) Gosztola, D.; Niemczyk, M. P.; Svec, W.; Lukas, A. S.; Wasielewski, M. R. *J. Phys. Chem. A* **2000**, *104*, 6545−6551.

orthogonal pyridine spacers.[47,48] Unlike rectangles **1**−**6**, cyclic voltammograms of **7** feature chemically irreversible reduction peaks, which are likely associated with reduction of the Re centers.

Spectroelectrochemistry: Visible and Infrared Regions. As shown in Figure 4 for **1** and **2**, the UV−visible absorption spectra of the neutral rectangles are dominated by high energy (300−400 nm) bands associated with intraligand (BiBzIm) transitions. In addition, spectra for **2** and **4** contain absorption bands from 400 to 500 nm, which are associated with the pyrz and diPyTz ligands. Ligand absorptions for **5** and **6** are higher in energy and are obscured by the BiBzIm transitions. Table S1 includes quantitative UV−visible absorption data for **1**−**6** in the 0, 1−, and 2− states. None of the molecular rectangles are detectably emissive in solution at ambient temperatures.[49]

Support for the assignments above of electrochemical reduction waves as LL based is provided by spectroelectrochemical measurements. As shown in Figure 4, when an appropriately negative potential is applied to reduce **1** to the 1− state, absorption bands at 396, 426, 598, and 644 nm evolve, indicating the presence of the radical anion form of the 4,4′-bpy ligand. The peaks are lower in energy than those reported for the anionic form of the free ligand[50] but closely approximate to those of the radical cation of methyl viologen.[51] The bands for **1** increase in intensity, as expected, upon reduction to the 2− state and formation of a second anionic bipyridine. Hartmann and Kaim have reported similar behavior for a cationic analogue of **1**.[43] Molecular rectangle **3**, in the 1− state, shows ligand absorptions at 468, 460, and 610 nm, similar to values reported for the *N,N*′-dimethyl-2,7-diazapyrene monocation.[52] In the singly reduced form of **4**, absorptions at 450, 476, and 718 nm match those of the *N,N*′-dimethyl-di-3,6-(4-pyridyl)-1,2,4,5-

(47) Hayes, R. T.; Wasielewski, M. R.; Gosztola, D. *J. Am. Chem. Soc.* **2000**, *122*, 5563−5567.
(48) Miller, S. E.; Lukas, A. S.; Marsh, E.; Bushard, P.; Wasielewski, M. R. *J. Am. Chem. Soc.* **2000**, *122*, 7802−7810.
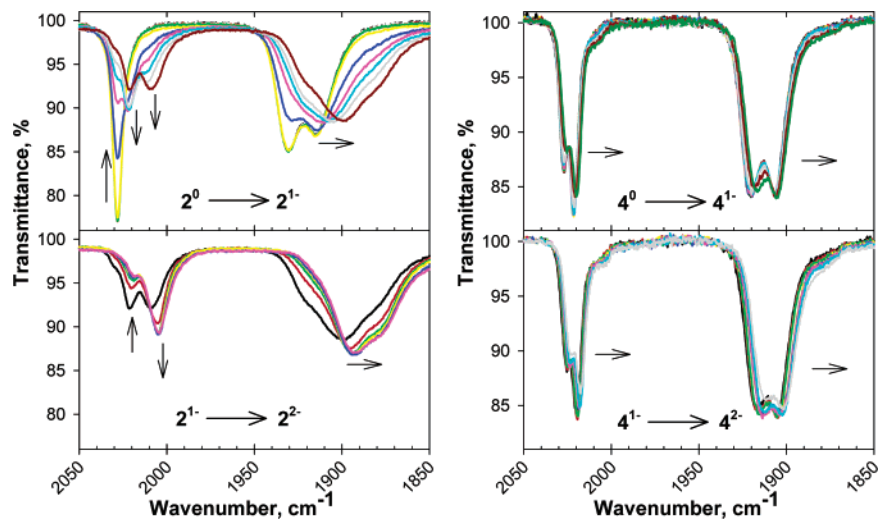(49) The luminecense reported for **1** in ref 6 is incorrect; the observed emission at ca. 600 nm was due to a contaminant.
(50) Shida, T. *Electronic Absorption Spectra of Radical Ions*; Elsevier: Amsterdam, 1988.
(51) Kosower, E. M.; Cotter, J. L. *J. Am. Chem. Soc.* **1964**, *86*, 5524−5527.
(52) Waldhoer, E.; Zulu, M. M.; Zalis, S.; Kaim, W. *J. Chem. Soc., Perkin Trans. 2* **1996**, 1197−1204.

Figure 5. IR-SEC scans in the carbonyl region for **2** (left) and **4** (right) taking in THF with 0.1 M TBAPF$_6$ as the supporting electrolyte. The top graphs show the reduction from the 0 to 1− state, and the bottom graphs show the reduction from the 1− to 2− state for each compound.

tetrazine monocation.[52] Finally, the ligand absorptions at 424, 494, 652, and 718 nm, for **5**$^{1-}$, and 458, 564, 612, and 780 nm, for **6**$^{1-}$, parallel those of radical anions of closely related di-*tert*-butylphenyl substituted benzenediimide and naphthalene-diimide species.[46] Absorption spectra for **3**−**6**, in the neutral, 1− and 2− states, are shown in Figure S1.

Somewhat different behavior was encountered for **2** (Figure 4). A weak band at 422 nm, assigned as a rhenium-to-pyrazine charge-transfer band, decreases in intensity upon reduction to the 1− state. An even weaker band, now at somewhat lower energy, is observed for the 2− form. Its origin is uncertain, but assignment as a ligand-centered (pyrazine anion) transition is one possibility.

SEC measurements for **1**−**6** were also made in the CO vibrational region of the infrared spectrum. Stretching frequencies for carbonyls are well-known to report on relative electron densities at coordinated metal centers, generally moving lower as electron density increases. Figure 5 shows the IR-SEC data for **2** and **4**. The reduction of **2** to the 1− state breaks the D_{2h} symmetry, and two new bands appear at 2022 and 2009 cm^{-1}. The bands around 1925 cm^{-1} are shifted to lower energy but are not as well resolved. As the rectangle is further reduced to the 2- state, the symmetry is restored and only three bands are present, now at 2007, 1892, and 1879 cm^{-1}. In contrast, the addition of an electron to **4** does not affect the local symmetry of the Re(CO)$_3$ units sufficiently to generate resolvable new bands. All four bands of the neutral complex shift to progressively lower energy upon reduction to the 1− and then 2− states. IR-SEC data for **1** and **3** are similar to those of **4**, but with larger shifts. The magnitudes of the shifts in stretching frequency, $\Delta\nu$(CO), are highly dependent on the size of the ligand reduced. As shown in Figure 6, where average $\Delta\nu$(CO) values for the neutral versus 2− state of each rectangle are plotted versus the area of LL, the smallest ligands engender the largest shifts. The effect can be understood, in part, in terms of dilution of the added charge on the metal-bound nitrogen atoms by delocalization over the entire ligand. Additionally, for **5** and **6** where shifts are small (<4 cm^{-1}), the reductions are likely largely confined to the central tetracarboxydimide dianhydride fragments, making the charge changes at the pyridyl nitrogens small.
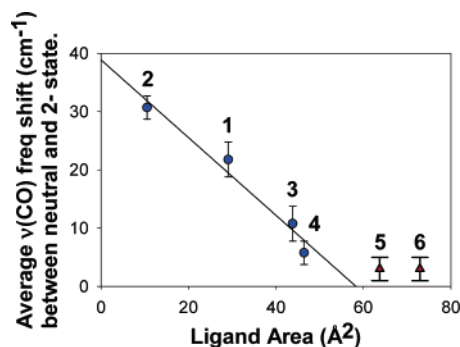
Figure 6. Plot of average CO frequency shifts between neutral and 2− states versus the area of the bridging ligand for **1**−**4** (blue circles) and **6** and **7** (red triangles). The solid line represents the linear regression for **1**−**4**. The plot illustrates the effect of charge localization on the bridging ligands and Re(CO)$_3$ centers as the size of the ligand increases. For **6** and **7**, the charge is localized on the central tetracarboxydimide rings. For these two, the nominally orthogonal pyridyl linkers restrict electronic communication with the Re(CO)$_3$ centers (see semiempirical modeling below).
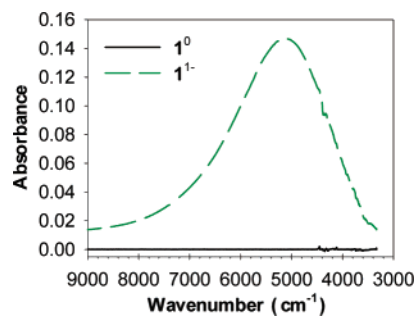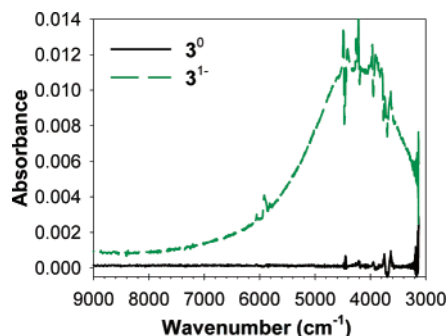

Figure 7. NIR absorption scans for a 5.3×10^{-4} M solution of **1** in THF with 0.1 M TBAPF$_6$. The neutral state is shown as a solid black line, and the 1− state, as a dashed green line.

Spectroelectrochemistry: Near-Infrared Regions. SEC measurements were also made for **1**−**6** in the near-infrared (NIR) region of the spectrum. Figures 7 and 8 contain spectra obtained for **1** and **3** in THF and CH$_2$Cl$_2$, respectively. The spectra reveal broad absorption bands centered at 5115 cm^{-1} for **1**$^{1-}$, and 4255 cm^{-1} for **3**$^{1-}$. The bands disappear upon further reduction to the 2− state or upon restoration of the neutral form. (Absorption spectra for the 2− state are not shown due to difficulties in achieving full conversion to the doubly

Table 4. IT Band Absorption Data, Charge-Transfer Distances, and Calculated Electronic Coupling

rectangle	ν_{max} (cm^{-1})	ϵ (M^{-1} cm^{-1})	$\Delta\nu_{1/2,measd}$ (cm^{-1})	$\Delta\nu_{1/2,calcd}$ (cm^{-1})	$R_{geom,calcd}$ (Å)	μ_{12} (eÅ)	R_{12} (Å)	R_{ab} (Å)	H_{ab} (cm^{-1})	α	solvent
1^{1-}	5115	3000	2230	3440	5.0	0.75	3.6	3.9	1000	0.20	THF
2^{1-}	5350	150	4500	3520	5.6	0.23	3.2	3.3	400	0.07	THF
3^{1-}	4255	1300	2060	3140	4.3	0.52	3.6	3.8	600	0.14	CH$_2$Cl$_2$
4^{1-}	6595	1100	3385	3900	4.9	0.49	3.7	3.9	800	0.12	THF

Figure 8. NIR-SEC absorption scans for an 8.8×10^{-5} M solution of **3** in CH$_2$Cl$_2$ with 0.1 M TBAPF$_6$. The neutral state is shown as a solid black line, and the 1− state, as a dashed green line. The spikes in the absorption spectra result from imperfect subtraction of absorption due to solvent and electrolyte vibrational overtones.

reduced forms; typically only about 80−90% conversion was obtained.) These bands clearly are electronic and are assigned as ligand-based intervalence transitions (IT). Bands were also found for assemblies **2**$^{1-}$ and **4**$^{1-}$ but were not detected for **5**$^{1-}$ or **6**$^{1-}$ (nor were they observed for any of the triply reduced rectangles). Table 4 contains IT band absorption data for **1**$^{1-}$, **2**$^{1-}$, **3**$^{1-}$, and **4**$^{1-}$.

Mixed Valence Analysis: Electrochemistry. The difference in formal potential, ΔE_f, for identical redox sites reflects not only electrostatic effects, as noted above, but also the degree of electronic communication between the sites. By defining the diabatic initial state of the 1− assembly as one with the added electron fully localized on one of the two ligands, LL, and the final state as one with the electron fully localized on the other, the initial-state/final-state coupling energy, H_{ab}, contributes the quantity H_{ab}^2/λ to the difference in formal potential.[53,54] On this basis, the electronic coupling energy for **6**$^{1-}$ clearly must be moderate or small.

Regardless of its origin, K_c is a direct measure of the thermodynamic stability of the mixed valence species with respect to disproportionation into unreduced and doubly reduced forms:

$$2[0,-1] \xrightleftharpoons{K_c^{-1}} [0,0] + [-1,-1] \qquad (2)$$
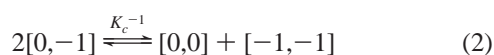
Expressed instead in terms of comproportionation, the relation is

$$K_c = \frac{[0,-1]^2}{[0,0] \times [-1,-1]} = e^{\Delta EF/RT} \qquad (3)$$

where F is the Faraday constant. Table 3 lists K_c values for the six singly reduced mixed-valence rectangles. These values vary significantly with the identity of the bridging ligand and broadly

parallel the extent of ligand van der Waals interactions implied by the X-ray crystal structures. K_c values for the rectangles are included in Table 3 for the formation of the 1− MV state. Compounds **3** and **4** have the highest values for K_c, 1.2×10^6 and 8.2×10^5, respectively, implying a significant amount of electrostatic communication between reduced ligands. The crystal structures of these two rectangles (in neutral form) show the central bridging ligands in close proximity, near van der Waals contact (Figure 2), allowing for strong interaction between ligands.

The values for **1**, **2**, and **5** are somewhat lower: 7.7×10^3, 3.7×10^4, and 1.7×10^4, respectively. The X-ray crystal structures of **1** and **2** reveal more rigid structures than those of **3** and **4**, maintaining larger LL/LL separation distances. In the case of **1**,[6] the dihedral displacements of pyridyl rings in relation to each other enable the assembly to sustain linear N−N (LL) axes, while the short length of the pyrazine ligand prevents the inward bowing seen in **3** and **4**. In the structure of **5**, the spacial proximity of the ligands presumably facilitates electrostatic communication, but the horizontal offset of central rings keeps K_c from reaching the values of **3** and **4**. Like **5**, the central naphthalene rings of molecular rectangle **6** are in contact, but it still is characterized by the smallest K_c value (30) of all the rectangles examined. One factor may be the large horizontal offset between the central rings. Another may be the larger LL area, compared to **2** for example, over which the charge may disperse, thereby reducing charge density and electrostatic repulsions.

For three of the rectangles, the table also lists values for formation of a second mixed-valence form, a triply reduced assembly; K_c' eq 4.

$$2[-1,-2] \xrightleftharpoons{K_c'^{-1}} [-1,-1] + [-2,-2] \qquad (4)$$
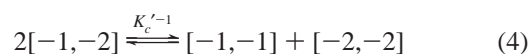
(Suitable electrochemical data were not obtained for the other three.) In each case, the 3− MV form is less stable than the 1− form. From Coulomb's law, the electrostatic contribution to the comproportionation free energy should scale as the difference in charge products for the redox sites divided by the distance separating them. For the singly reduced form, the charge scaling is nominally $|(1-)(0) - 0.5[(0)(0) + (1-)(1-)]| = 0.5$. For the triply reduced form, the charge scaling is nominally the same: $|(2-)(1-) - 0.5[(1-)(1-) - (2-)(2-)]| = 0.5$. The separation distance, however, clearly should be greater for the 3− form because of the LL/LL Coulombic repulsion present there but absent for the 1− form. Additionally, double reduction of LL is likely to increase the contribution of quinoidal resonance forms to the geometric and electronic structure of the ligand. Quinoidal structures should be more rigid than nonquinoidal ones. This effect should rigidify the rectangular structure, increase the interligand separation distance and thereby decrease the electrostatic contribution to K_c. Finally, increases in separation distance will decrease H_{ab} and further diminish

(53) Sutton, J. E.; Sutton, P. M.; Taube, H. *Inorg. Chem.* **1979**, *18*, 1017− 1021.

(54) Sutton, J. E.; Taube, H. *Inorg. Chem.* **1981**, *20*, 3126−3134.
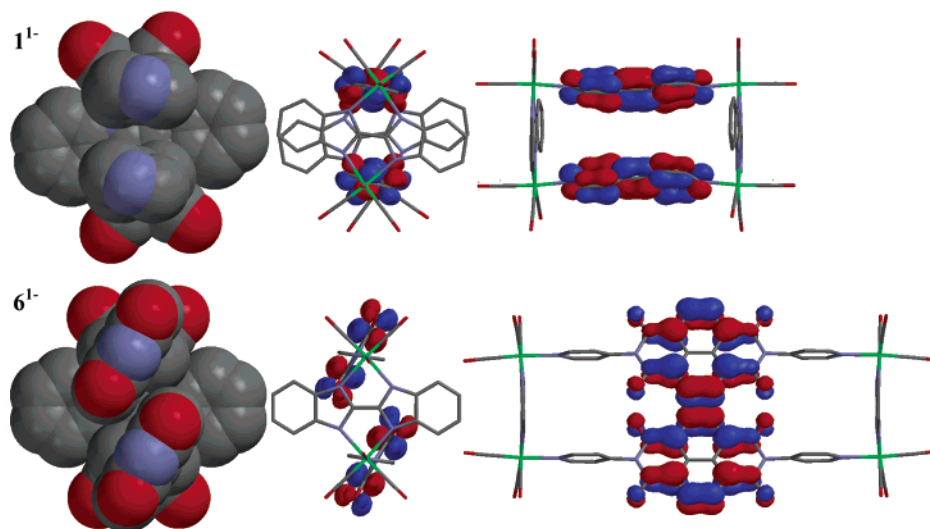
Figure 9. PM3(tm)/UHF semiempirical geometry optimized structures of $\mathbf{1}^{1-}$ (top) and $\mathbf{6}^{1-}$ (bottom). Carbon atoms are shown in gray, nitrogen, in blue, oxygen, in red, and rhenium, in green; the hydrogen atoms were removed for clarity. In both structures, the reduced ligand is on top. The left most images are space filled models, viewed along the long axis of the rectangles, with the nearest [Re(CO)$_3$]$_2$BiBzIm (and pyridyl units for $\mathbf{6}^{1-}$) removed for clarity. The middle and right images are stick models displaying the HOMO (centered on top ligand) and LUMO (centered on bottom ligand) orbitals.

K_c. Notably, none of the 3− forms displayed detectable intervalence absorption intensity.

Mixed Valence Analysis: Spectroelectrochemistry. Intervalence band energies (ν_{max}) and intensities (ϵ_{max}) can be used to estimate H_{ab}. For class II compounds, assuming a two-state description in the classical limit, Hush has derived the following:

$$H_{ab} = \frac{0.0206}{R_{ab}}\sqrt{\nu_{max}\epsilon_{max}\Delta\nu_{1/2}} \qquad (5)$$

where R_{ab} is the diabatic electron-transfer distance and $\Delta\nu_{1/2}$ is the observed bandwidth at half-height.[55,56] Additionally, the band energy can be equated with the diabatic reorganization energy, λ. In the class III limit (valence-delocalized limit; $2H_{ab} > \lambda$), the relation is simpler:

$$H_{ab} = \nu_{max}/2 \qquad (6)$$

Application of eq 5 requires estimates for R_{ab}. Uses of geometric LL/LL separation distances, R_{geo}, determined crystallographically for the neutral compounds, are most likely incorrect. Crystal packing forces may alter the LL/LL separation, and the addition of electrons to the rectangles will most likely engender other structural changes. At the same time, direct electronic Stark effect measurements of the diabatic charge-transfer distance often show that R_{geo} *over*estimates R_{ab}.[57−62]

In light of these facts, we employed PM3(tm)/UHF semiempirical modeling to gain insight into the structures of the anionic forms of these rectangles. Figure 9 shows the PM3(tm)/UHF geometry-optimized structures for the radical anions of **1** and **6**. Except for **2**, the LL/LL separation distances of the monoan-

ionic assemblies exceed those obtained crystallographically for the neutral assemblies.

In **1**, the reduced form of 4,4′-bpy is predicted to adopt a planar quinoidal structure as has been observed with the radical cation of methyl viologen.[63−65] The geometry-optimized structure (Figure 9) clearly shows a decrease in dihedral angle between pyridine rings of the reduced side of the rectangle (21°, versus 39° for the neutral side, bottom). The planarity of the reduced 4,4′-bpy ligand engenders more rigidity in the rectangle structure, increasing the minimum LL/LL separation distance from 3.9 to 5.0 Å. Increases in LL/LL separation are also seen in the calculated monoanionic structures of **3** and **4**. In both X-ray crystallographic structures, the nominally planar bridging ligands bow inward sufficiently to achieve van der Waals contact, but in the semiempirical models of the corresponding 1- compounds, the bridging ligands become more rigid, enlarging the LL/LL separation distance. Unlike **1**, **3**, and **4**, the changes for **2** are minimal. The pyrazine−pyrazine distance is approximately 5.3 Å in the X-ray crystal structure and 5.6 Å in the calculated monoanionic structure.

The calculated anionic structures of **5** and **6** help elucidate the lack of observable intervalence absorption in NIR-SEC experiments. In both mixed-valence structures, the central tetracarboxydiimide rings shift laterally in relation to each other, in addition to spreading apart. These structural changes result in less than 25% and 10% cofacial area overlap for **5** and **6**, respectively, likely accounting for the lack of optically significant electronic coupling. Additionally, the calculated HOMO and LUMO orbitals for **5** and **6** (Figure 9) reveal nodes at the diimide nitrogen positions of the central rings, effectively eliminating electronic communication between the central rings and the Re-coordinating pyridyl groups. This is consistent with the relatively small differences in reduction potentials between the rectangle-coordinated and free versions of the ligand and the minute CO frequency shifts seen in IR-SEC measurements.

(55) Hush, N. S. *Prog. Inorg. Chem.* **1967**, *8*, 391−444.
(56) Hush, N. S. *Coord. Chem. Rev.* **1985**, *64*, 135−157.
(57) Vance, F. W.; Williams, R. D.; Hupp, J. T. *Int. Rev. Phys. Chem.* **1998**, *17*, 307−329.
(58) Shin, Y. G. K.; Brunschwig, B. S.; Creutz, C.; Sutin, N. *J. Am. Chem. Soc.* **1995**, *117*, 8668−8669.
(59) Shin, Y. K.; Brunschwig, B. S.; Creutz, C.; Sutin, N. *J. Phys. Chem.* **1996**, *100*, 8157−8169.
(60) Oh, D. H.; Boxer, S. G. *J. Am. Chem. Soc.* **1990**, *112*, 8161−8162.
(61) Oh, D. H.; Sano, M.; Boxer, S. G. *J. Am. Chem. Soc.* **1991**, *113*, 6880−6890.
(62) Reimers, J. R.; Hush, N. S. *J. Phys. Chem.* **1991**, *95*, 9773−9781.

(63) Hester, R. E.; Suzuki, S. *J. Phys. Chem.* **1982**, *86*, 4626−4630.
(64) Poizat, O.; Sourisseau, C.; Corset, J. *J. Mol. Struct.* **1986**, *143*, 203−206.
(65) Wolkers, H.; Stegmann, R.; Frenking, G.; Dehnicke, K.; Fenske, D.; Baum, G. *Z. Naturforsch., B: Chem. Sci.* **1993**, *48*, 1341−1347.

Table 4 lists the minimum LL/LL separation distances, $R_{geom,calc}$, determined semiempirically for the singly reduced forms of the rectangles. These distances are not necessarily equivalent to the required diabatic charge-transfer distances, R_{ab}. To estimate R_{ab} we first made used of the PM3(tm)/UHF semiempirical calculations to determine the ground-state dipole moment, μ_g, for each rectangle. We, along with Nelsen and Newton, have shown elsewhere under certain conditions,[66] the adiabatic charge-transfer distance, R_{12}, can be directly equated with $2\mu_g$ (in other words, the *change* in dipole moment for the transfer of an electron).[67-69] The PM3(tm)/UHF semiempirically calculated ground-state dipole moments for 1^{1-}, 2^{1-}, 3^{1-}, and 4^{1-} are 1.79, 1.62, 1.82, and 1.87 eÅ respectively. These were then converted to diabatic distances (R_{ab}) using experimental intervalence energy and oscillator strength parameters, by the generalized Muliken–Hush analysis as prescribed by Cave and Newton.[70,71] Briefly, the change in diabatic charge-transfer distance can be determined from eq 7

$$R_{ab} = \sqrt{(R_{12})^2 + 4(\mu_{12})^2} \qquad (7)$$

where μ_{12} is the transition dipole moment in eÅ, as estimated via eq 8 from the intervalence absorption parameters.

$$\mu_{12} = \sqrt{\frac{\epsilon_{max}\,\Delta\nu_{1/2}}{\nu_{max}}} \qquad (8)$$

Table 4 summarizes the distances obtained in this way. Notably, both the diabatic and adiabatic charge-transfer distances are shorter than the geometric donor–acceptor separation distances, $R_{geom,calcd}$. Table 4 also lists the electronic coupling energies obtained from eq 5 using the calculated adiabatic charge-transfer distances and measured intervalence absorption spectra. Also listed are estimates of α, Hush's delocalization parameter, the amount of charge already transferred from donor site to acceptor site in the ground electronic state. These were obtained (again using the simple Hush theory) from

$$\alpha = H_{ab}/\nu_{max} \qquad (9)$$

All of the singly reduced rectangles appear to be valence-localized assemblies. We tentatively assign 1^{1-}, 2^{1-}, 3^{1-}, and 4^{1-} as class II species and 5^{1-} and 6^{1-} as borderline class I species.[72,73] Also assigned as borderline class I, based on the absence of observable IT bands, are the triply reduced versions on the rectangles.

Hush also has derived an expression, applicable to class II species, that relates intervalence bandwidth to band energy in the classical limit:[55]

$$\Delta\nu_{1/2} = \sqrt{16\ln(2)k_{B}T\nu_{max}} \qquad (10)$$

Absorption bands for 1^{1-} and 3^{1-}, in particular, are narrower than expected (ca. 3400 and 3100 cm^{-1} calculated), while the IT band for 2^{1-} is wider than expected (ca. 3600 cm^{-1} calculated). Additionally, the line shapes for 1^{1-}, 3^{1-}, and 4^{1-} deviate from the Gaussian ideal, being narrower on the low-energy side than on the high-energy side. The asymmetry could signal the coupling of significant vibrational reorganization to the intervalence excitation. Alternatively, the asymmetry might be a manifestation of the "$2H_{ab}$ cutoff" effect described by Lambert and Nöll for classical systems, although the estimated electronic coupling energies appear to be too small for the cutoff effect to be important.[29,74,75] Experimentally, narrower than expected line shapes are often encountered when class II systems approach the class III limit, conditions where the Born–Oppenheimer condition may fail and intervalence excitation may entail significant vibronic coupling. Notably, vibronic coupling treatments typically predict narrower intervalence line shapes than does Hush theory.[76] In the pyrazine-based mixed-valence assembly, 2^{1-}, the wider than expected bandwidth might reflect problems in background spectral subtraction for this weakly absorbing assembly, rather than a real discrepancy. If so, then the estimate for H_{ab} should be revised downward by ~25%.

To gain additional insight into the significance of the estimated electronic coupling energies, specifically in the context of ground-state intramolecular electron transfer, adiabatic and diabatic potential-energy surfaces were compared. Figure 10 shows the results for rectangles 1^{1-} and 3^{1-}. The surfaces were generated using Hush theory[29] using data contained in Table 4. (Specifically, eqs 1a, 1b, 3a, and 3b of ref. [29] were employed.) While a double-welled ground potential-energy surface is retained in both cases, considerable barrier rounding exists for electron exchange within 1^{1-}. For 2^{1-} the perturbation is much smaller but still large enough to ensure adiabatic electron exchange.

The coupling-energy estimates for the six mixed-valent rectangles are broadly consistent with expectations from crystallographic studies and semiempirical radical anion geometry optimizations. The most strongly coupled systems, **1**, **3**, and **4**, are characterized in the neutral state by van der Waals (or near

(66) We assume, as is usually done, that R_{12} for thermal electron-transfer equals R_{12} for optical electron transfer (a condition likely satisfied for two-state systems). Under these circumstances, μ_g is equal to $-\mu_e$ (the dipole moment for the intervalence excited state) provided that (1) a mirror plane exists, (2) the plane lies between the donor site and the acceptor site, and (3) the coordinate origin for dipole determination is located in the plane. The vector difference between μ_g and μ_e (μ_g and $-\mu_g$) then equals R_{12} after conversion from units of debye to units of eÅ. The mixed-valence rectangles are very well approximated by structures featuring mirror planes.
(67) Electronic Stark effect methods can provide direct experimental measures of charge-transfer induced changes in dipole moment and, therefore, R_{12}. The measurements require rigid matices so that field-induced reorientation of chromophores is prevented. Attempts to apply the technique to singly reduced rectangles were largely unsuccessful. In most cases the compounds reversibly disproportionated into neutral and doubly reduced compounds when low-temperature glass formation was attempted. A possible cause may be diminished solubility and precipitation of one of the forms at low temperature. In two of six attempts with **1**, disproportionation at 77 K° was avoided and intervalence Stark spectra were recorded. The experiments and subsequent analysis yielded $R_{12} = 1.5$ eÅ and $R_{ab} = 2.1$ eÅ. The values are somewhat smaller than those obtained from semiempirical calculations and used in eq 5, suggesting that the assembly, while still a class II species, is more strongly coupled than that indicated in the table. Using the Stark data, admittedly from experiments that have been difficult to reproduce, alternative estimates for H_{ab} and α are 1830 cm^{-1} and 0.36.
(68) Johnson, R. C.; Hupp, J. T. *J. Am. Chem. Soc.* **2001**, *123*, 2053−2057.
(69) Nelsen, S. F.; Newton, M. D. *J. Phys. Chem. A* **2000**, *104*, 10023−10031.
(70) Cave, R. J.; Newton, M. D. *Chem. Phys. Lett.* **1996**, *249*, 15−19.
(71) Cave, R. J.; Newton, M. D. *J. Chem. Phys.* **1997**, *106*, 9213−9226.

(72) We interpret the absence of detectable intervalence absorption by 5^{1-} and 6^{1-} as evidence that H_{ab} is considerably less than 400 cm^{-1} and probably less than 100 cm^{-1}. 100 cm^{-1} would be more than sufficient, however, to ensure adiabatic thermal electron exchange kinetics. Indeed, dependent on the nature of the exchange reaction dynamics, as little as 60 cm^{-1} would be sufficient. 5^{1-} and 6^{1-} may well be class I like only in an optical sense.
(73) With these estimates, the issue of electronic-coupling contributions to electrochemical potential differences, ΔE_f, can be revisited. Estimating these contributions as H_{ab}^2/ν_{max}, the values are small, ranging from ~3 mV for **2** to ~24 mV for **1**.
(74) Lambert, C.; Noll, G. *J. Am. Chem. Soc.* **1999**, *121*, 8434−8442.
(75) Nelsen, S. F. *Chem.−Eur. J.* **2000**, *6*, 581−588.
(76) Coropceanu, V.; Malagoli, M.; Andre, J. M.; Bredas, J. L. *J. Am. Chem. Soc.* **2002**, *124*, 10519−10530.
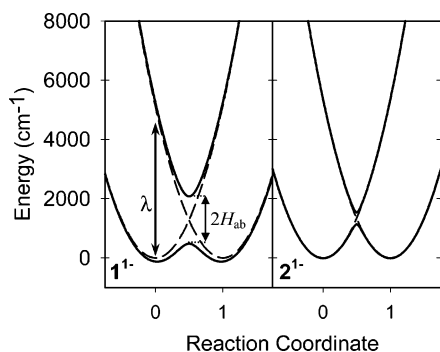
Figure 10. Calculated potential energy surfaces for $\mathbf{1}^{1-}$ (left) and $\mathbf{2}^{1-}$ (right) based on the two-state Hush model. Adiabatic surfaces are shown as solid lines, and diabatic surfaces, as dashed lines. The values for $\lambda = \nu_{max}$ and H_{ab}, for $\mathbf{1}^{1-}$ and $\mathbf{2}^{1-}$, were taken from Table 4.

van der Waals) contact between LL pairs, at least near the centers of the ligands. While the LL/LL separation distances (calculated) are somewhat greater for the mixed-valence rectangles, the ligands remain relatively planar and in good spatial overlap to facilitate direct electronic interaction. The weakly coupled systems, **5** and **6**, also achieve van der Waals contact in the neutral state but are offset in a fashion that reduces LL/LL π^*-orbital overlap. Rectangle **2**, which is weakly but detectably coupled, is constrained by ligand size and rigidity from achieving LL/LL contact and good donor/acceptor orbital overlap.

Finally, the comparatively small value of H_{ab} for the pyrazine based rectangle, **2**, in comparison to its value for **1**, **2**, and **5**, strongly suggests that coupling for the latter three is obtained primarily by direct LL/LL orbital overlap rather than through rhenium-mediated superexchange. The H_{ab} value for **3** can be taken as an upper limit estimate of coupling obtainable by superexchange. The rigid pyrazine ligand, comprising a single ring doubly ligated to rhenium ions, represents an optimal moiety for participation in superexchange, to the extent that it can occur in a molecular rectangle configuration.

Conclusions

The molecular rectangles described here are examples of a new type of ligand-centered mixed-valence compound that employs a metal-organic framework to arrange the redox active ligands in a manner that controls, at least in part, spatial overlap and through-space interactions and, thus, electronic communication. X-ray crystallographic studies of the rectangles, in neutral form, reveal a range of LL/LL geometrical configurations with minimum interligand distances varying from van der Waals contact (ca. 3.3 Å) to 5.3 Å. Cyclic voltammetry experiments reveal chemically reversible single electron reductions that allow for the addition of two to four electrons per rectangle. UV–visible and IR-SEC measurements establish that the reductions are LL based.

The singly and triply reduced assemblies are mixed-valence species. For the triply reduced species, and two of the six singly reduced, electronic coupling is weak as evidenced by the absence of detectable intervalence absorption bands. Four of the singly reduced LCMV species, however, do display weak ($\epsilon = 150$ M^{-1} cm^{-1}) to moderately intense ($\epsilon = 3000$ M^{-1} cm^{-1}) intervalence absorption bands in the extended near-infrared region. We find that electronic coupling is chiefly governed by through-space LL/LL interactions, with the Re atoms and

associated double-chelating ligands largely limited to a structural role. For these six systems, variations in coupling strength lead to mixed-valence behavior ranging from nearly Class I (non-communicating, fully valence-localized redox centers) to strongly Class II on the Robin and Day scale, or roughly a 100-fold variation in H_{ab}^2 despite nominally identical coordination-defined geometries and the absence of any bridging unit. The observed differences largely reflect detailed geometric configurational differences that can either facilitate of frustrate productive direct orbital overlap. Because coupling is attained primarily by direct donor-orbital/acceptor-orbital overlap (rather than superexchange) and because mixed valency is based on ligands rather than transition metal ions, the rectangles comprise systems that can be logically described by Hush's idealized two-state model.

Experimental Section

General Methods. Infrared spectra were recorded on a Bio-Rad FTS-40 FTIR spectrometer. All NMR spectra were recorded on either a Varian Mercury-400 MHz or Varian INOVA-500 MHz spectrometer, and the chemical shifts were referenced to the standard solvent shift. FAB LRMS were obtained in the Mass Spectrometry Laboratory, School of Chemical Sciences, University of Illinois. Elemental analyses were performed by Atlantic Microlabs, Inc. Norcross, GA. UV–vis–NIR absorption spectra were measured using a Varian Cary 5000 spectrometer. MALDI LR-MS were performed using a Perspective Biosystems, Voyager DE-Pro MALDI-TOF. EI LRMS and HRMS were performed using a VG70-250SE high-resolution mass spectrometer.

Materials. All commercial reagents were of ACS grade and used without further purification. Tetrahydrofuran (THF), methylene chloride, and dimethyl sulfoxide (DMSO) were purified using a two-column solid-state purification system (Glasscontour System, Joerg Meyer, Irvine, CA). 4-Aminopyridine, 1,4,5,8-naphthalenetetracarboxylic, 1,2,4,5-benzenetetracarboxylic, pyrazine, and 4-cyanopyridine were purchased from Aldrich. Hydrazine monohydrate was purchased from Fisher Scientific. [Re(CO)$_4$]$_2$BiBzIm (**2**),[6] 2,7-diazapyrene,[77,78] and **1**[6] were synthesized by literature procedures.

Di-3,6-(4-pyridyl)-1,2,4,5-tetrazine (8). 4-Cyanopyridine (5.5 g, 52.8 mmol), hydrazine monohydrate (25 mL), concentrated HCl (5 mL), and deionized water (5 mL) were refluxed together for 2 h. After the mixture cooled, 4.9 g of the orange, dihydro intermediate was isolated by filtration. The precipitate was immediately added to 200 mL of glacial acetic acid with stirring. A 35 mL aliquot of 30% HNO$_3$ was added dropwise to the brown solution. The reaction mixture turned pink, and the oxidized product was isolated as the HNO$_3$ salt by filtration. Recrystallization from pyridine gave 3.44 g of the purple product (52% overall yield). ^{1}H NMR (400 MHz, CDCl$_3$) 8.96 (d, $J =$ 5 Hz, 4H), 8.52 (d, $J =$ 5 Hz, 4H). ^{13}C NMR (400 MHz, CDCl$_3$) 163.5, 151.1, 138.5, 121.3. EI-LRMS (m/z): [M]+ calcd for C$_{12}$H$_8$N$_6$: 236.2, found 236.2. EI-HRMS (m/z): [M]+ calcd for C$_{12}$H$_8$N$_6$: 236.0810, found 236.0809. Anal. Calcd for C$_{12}$H$_8$N$_6$: C, 61.01; H, 3.41; N, 35.58. Found: C, 60.64; H, 3.36; N, 35.60.

***N,N′*-Di-(4-pyridyl)-1,2,4,5-benzenetetracarboxydiimide (9).** 1,2,4,5-Benzenetetracarboxylic dianhydride (1.0 g, 4.6 mmol) and 4-aminopyridine (1.08 g, 11.5 mmol) were added to a reaction flask. Anhydrous dimethylformamide (DMF, 50 mL) (Aldrich) was added under N$_2$, and the solution was refluxed overnight under N$_2$. After the reaction mixture cooled in an ice bath, the white slurry was filtered and the product was washed with CH$_2$Cl$_2$ and acetone. The product was then dried under vacuum to yield 716 mg of a white powder (42% yield). ^{1}H NMR

(77) Stang, P. J.; Cao, D. H.; Saito, S.; Arif, A. M. *J. Am. Chem. Soc.* **1995**, *117*, 6273−6283.
(78) Huenig, S.; Gross, J.; Lier, E. F.; Quast, H. *Justus Liebigs Ann. Chem.* **1973**, 339−358.

(400 MHz, CF$_3$COOD) δ 8.90 (d, *J* = 5 Hz, 4H), 8.80 (d, *J* = 5 Hz, 4H), 8.73 (s, 2H). ^{13}C NMR (400 MHz, CF$_3$COOD) δ 165.7, 151.6, 144.7, 139.4, 123.7, 122.8. MS-MALDI-TOF (*m/z*): [MH]+ calcd for C$_{20}$H$_{10}$N$_4$O$_4$: 371.3; found 371.1. Anal. Calcd for C$_{20}$H$_{10}$N$_4$O$_4$: C, 64.87; H, 2.72; N, 15.13. Found: C, 64.63; H, 2.70; N, 14.94.

N,N′-Di-(4-pyridyl)-1,4,5,8-naphthalenetetracarboxydiimide (10). Using the same procedure as that for **9**, combining 1,4,5,8-naphthalenetetracarboxylic dianhydride (1.0 g, 3.7 mmol) and 4-aminopyridine (770 mg, 8.2 mmol) produced 1.29 g of **10** (82% yield). ^{1}H NMR (500 MHz, CF$_3$COOD) δ 9.12 (d, *J* = 5 Hz, 4H), 9.03 (s, 4H), 8.37 (d, *J* = 5 Hz, 4H). ^{13}C NMR (500 MHz, CF$_3$COOD) δ 164.9, 154.8, 145.2, 135.0, 131.4, 129.7, 128.8. MS-MALDI-TOF (*m/z*): [MH]+ calcd for C$_{24}$H$_{12}$N$_4$O$_4$: 421.1; found 421.4. Anal. Calcd for (C$_{24}$H$_{12}$N$_4$O$_4$)-(H$_2$O): C, 65.75; H, 3.22; N, 12.78. Found: C, 66.35; H, 3.03; N, 12.90.

General Rectangle Synthesis. Compounds **2**−**6** were synthesized according to the method described by Benkstein, et al..^{6} Briefly, stoichometric amounts of **2** and the bridging ligand, LL, were combined with anhydrous THF (approximately 1−2 mL per mg of **2**) under N$_2$, and the reaction mixture was refluxed for 2 days under N$_2$. Removal of ca. 75% of the THF and addition of either diethyl ether or hexanes followed by filtration yielded the pure rectangle structures.

([Re(CO)$_3$]$_2$BiBzIm)$_2$-μ,μ′-(pyrazine)$_2$ (2). Compound **7** (114 mg, 0.14 mmol) and pyrazine (11 mg, 0.14 mmol) yielded 51 mg of **3** (43% yield) as a red powder. IR (THF, cm^{-1}) 2027 (C≡O), 1928 (C≡O), 1915 (C≡O). ^{1}H NMR (400 MHz, CD$_2$Cl$_2$) δ 8.12 (s, 8H), 7.73 (q, *J* = 3 Hz, 4H), 7.36 (q, *J* = 3 Hz, 4H). FAB LRMS, calcd *m/z* 1705.6, found *m/z* 1705.9. Anal. Calcd for Re$_4$C$_{48}$H$_{24}$N$_{12}$O$_{12}$: C, 33.80; H, 1.42; N, 9.85. Found: C, 34.73; H, 1.73; N, 9.44.

([Re(CO)$_3$]$_2$BiBzIm)$_2$-μ,μ′-(2,7-diazapyrene)$_2$ (3). Compound **7** (148 mg, 0.18 mmol) and 2,7-diazapyrene (36.5 mg, 0.18 mmol) yielded 138 mg of **2** as a yellow powder (79% yield). IR (CH$_2$Cl$_2$, cm^{-1}) 1907 (C≡O), 1922 (C≡O), 2024 (C≡O), 2027 (C≡O). ^{1}H NMR (500 MHz, CD$_2$Cl$_2$) δ 8.57 (d, *J* = 5 Hz, 8H), 8.02 (q, *J* = 3 Hz, 8H), 7.56 (q, *J* = 3 Hz, 8H), 7.19 (d, *J* = 5 Hz, 8H). FAB LRMS, calcd *m/z* 1953.9, found *m/z* 1954.0. Anal. Calcd for Re$_4$C$_{68}$H$_{32}$N$_{12}$O$_{12}$: C, 41.80; H, 1.65; N, 8.60. Found: C, 41.67; H, 1.71; N, 8.34.

([Re(CO)$_3$]$_2$BiBzIm)$_2$-μ,μ′-(di-3,6-(4-pyridyl)-1,2,4,5-tetrazine)$_2$ (4). Compounds **7** (120 mg, 0.15 mmol) and **8** (34.2 mg, 0.15 mmol) yielded 141 mg of **5** as an orange powder (96% yield). IR (THF, cm^{-1}) 2027 (C≡O), 2021 (C≡O), 1921 (C≡O), 1906 (C≡O). ^{1}H NMR (400 MHz, CD$_2$Cl$_2$) δ 7.87 (d, *J* = 5 Hz, 8H), 7.60 (d, *J* = 5 Hz, 8H), 7.45 (q, *J* = 3 Hz, 8H), 7.15 (q, *J* = 3 Hz, 8H). FAB LRMS, calcd *m/z* 2017.9, found *m/z* 2018.7. Anal. Calcd for Re$_4$C$_{64}$H$_{32}$N$_{20}$O$_{12}$: C, 38.09; H, 1.60; N, 13.88. Found: C, 60.64; H, 3.36; N, 35.60.

([Re(CO)$_3$]$_2$BiBzIm)$_2$-μ,μ′-(N,N′-di-(4-pyridyl)-1,2,4,5-benzenetetracarboxydiimide)$_2$ (5). Compounds **7** (80 mg, 0.09 mmol) and **9** (35.8 mg, 0.09 mmol) yielded 94 mg of **6** as an orange powder (85% yield). IR (THF, cm^{-1}) 2027 (C≡O), 2021 (C≡O), 1919 (C≡O), 1905 (C≡O). ^{1}H NMR (400 MHz, DMSO-*d$_6$*) δ 8.16 (d, *J* = 5 Hz, 8H), 8.01 (s, 4H), 7.82 (q, *J* = 3 Hz, 8H), 7.53 (q, *J* = 3 Hz, 8H), 7.32 (d, *J* = 5 Hz, 8H). FAB LRMS, calcd *m/z* 2286.1, found *m/z* 2287.0. Anal. Calcd for (Re$_4$C$_{80}$H$_{36}$N$_{16}$O$_{20}$)(H$_2$O): C, 41.70; H, 1.66; N, 9.73. Found: C, 41.97; H, 1.86; N, 9.32.

([Re(CO)$_3$]$_2$BiBzIm)$_2$-μ,μ′-(N,N′-dipyridyl-1,4,5,8-naphthalenetetracarboxydiimide)$_2$ (6). Compounds **7** (82.8 mg, 0.1 mmol) and **10** (42 mg, 0.1 mmol) yielded 91 mg of **7** as an orange powder (76% yield). IR (DMSO, cm^{-1}) 2024 (C≡O), 2018 (C≡O), 1911 (C≡O), 1903 (C≡O). ^{1}H NMR (400 MHz, DMSO-*d$_6$*) δ 8.28 (d, *J* = 5 Hz, 8H), 8.04 (s, 8H), 7.84 (q, *J* = 3 Hz, 8H), 7.52 (q, *J* = 3 Hz, 8H), 7.31 (d, *J* = 5 Hz, 8H). FAB LRMS, calcd *m/z* 2386.2, found *m/z* 2386.7. Anal. Calcd for (Re$_4$C$_{88}$H$_{40}$N$_{16}$O$_{20}$)(H$_2$O): C, 43.96; H, 1.76; N, 9.32. Found: C, 44.21; H, 1.97; N, 9.08.

Crystal Growth and Structure Determinations. X-ray quality crystals of **1**−**6** were grown over 5 to 10 day periods by slow diffusion of precipitating solvents into saturated solutions of the molecular

rectangles. Crystals of **1** were grown by diffusion of hexane into saturated THF. Crystals of **2** were grown by diffusion of cyclohexane into saturated 1,2-dichloroethane and THF. Crystals of **3** were grown by diffusion of hexanes into saturated CH$_2$Cl$_2$. Crystals of **4** were grown by diffusion of cyclohexane into a saturated 2-methyl-THF solution. Crystals of **5** were grown from the slow diffusion of cyclohexane into saturated THF. Crystals of **6** were grown by diffusion of methanol into saturated dimethyl sulfoxide. Crystals were mounted on glass fibers using oil and immediately placed in a cold nitrogen stream (153 K). Data collection was done using a Bruker Smart 1000 CCD diffractometer with Mo Kα radiation (λ = 0.710 69 Å) and processed using the SMART and SAINT programs.^{79} An analytical integration absorption correction was applied to all data. The structures were solved by direct methods. All structure solutions and refinement were done using the teXsan crystallographic software package. For all structures, non-hydrogen atoms were refined anisotropically and hydrogens were added in idealized positions. The refinements of all structures were straightforward. The crystallographic details are shown in Table 1. Additional information is provided in the Supporting Information.

Electrochemistry. All cyclic voltammetric experiments were performed and analyzed using a CHI900 (CH Instruments, Austin, TX) potentiostat. Electrolyte solutions (0.1 M tetrabutylammonium hexafluorophosphate (TBAPF$_6$) (>99%, Fluka)) were prepared with anhydrous solvents with and nitrogen degassed prior to use. A Pt wire was used as the counter electrode and a 2 mm diameter Pt or Au macro disk electrode was used as the working electrode. A silver wire was used as a pseudo-reference electrode, with ferrocene (Aldrich, purified by sublimation) added as an internal reference at the end of each experiment. All experiments were run under an nitrogen atmosphere.

Spectroelectrochemistry. Ultraviolet−visible−near-infrared spectroelectrochemical (UV−vis−NIR SEC) experiments were performed using a home-built optically transparent electrode. A 1 mm quartz cuvette was attached to a 14/20 ground joint with a stopcock and sample holding bulb. A ground joint containing three tungsten leads was used for the electrode connections. A Teflon coated wire was connected to a 5 mm × 15 mm Pt mesh working electrode, and a Pt wire was used as the counter electrode. The Ag wire pseudo-reference electrode was coated with Teflon shrink tubing so that only the bottom (15 mm) portion was exposed. The electrodes were arranged in the cell such that the Pt mesh was in the optical path of the quartz cuvette and the exposed portion of the Ag wire parallel to it. The Pt wire counter electrode was placed above the quartz cuvette area (ca. 2 cm away from the working electrode). Dry molecular rectangle and TBAPF$_6$ powders were added to the cell and thoroughly deoxygenated. Anhydrous solvent was then added, and the sample-electrolyte solution was freeze−pump−thaw degassed 4 times. NIR and UV−vis absorption scans were performed using a Varian CARY 5000 spectrometer while the cell potential was maintained with a Princeton Applied Research model 273 potentiostat.

IR SEC experiments were performed using a reflectance spectroelectrochemical cell based on a previously reported design.^{80} Spectra were recorded on a Bio-Rad FTS-40 FTIR spectrometer and the electrochemistry was controlled using a Princeton Applied Research model 273 potentiostat. Samples were prepared using anhydrous solvents with TBAPF$_6$ (>99%, Fluka) as the supporting electrolyte and freeze−pump−thawed three times prior to use. The solutions were transferred to the SEC cell under N$_2$ via airtight syringes. Blank spectra were recorded using the electrolyte solutions.

Molecular Modeling and Electronic Structure Calculations. PM3-(tm)/UHF semiempirical calculations were performed using PC Spartan Pro for Windows, Wave function Inc..^{81} Coordinates from the X-ray

(79) *SMART Version 5.054 Data Collection and SAINT-Plus Version 6.02A Data Processing Software for the SMART System*; Bruker Analytical X-ray Instruments: Madison, WI, 2000.
(80) Zavarine, I. S.; Kubiak, C. P. *J. Electroanal. Chem.* **2001**, *495*, 106−109.
(81) *PC Spartan Pro, version 1.0.5 for Windows*; Wave function Inc.: Irvine, CA 62612, 2000.

crystal structures were used as starting points for the geometry optimizations for the neutral and radical anion molecules. The center of mass was used as the coordinate of origin for the ground-state dipole moment calculations.

Supporting Information Available: UV−visible absorption spectra for **3**−**6** in the 0, 1−, and 2− states and quantitative UV−visible absorption data for **1**−**6** in the 0, 1−, and 2− states. X-ray crystallographic files for **1**−**6** (CIF). This material is available free of charge via the Internet at http://pubs.acs.org.

JA0473182